



RESEARCH ARTICLE

10.1029/2018JF004736

Sand Suspension and Transport During Inundation of a Dutch Barrier Island

Key Points:

- Suspended sand concentrations and transport are highly variable during and between inundation events on a Dutch barrier island
- Most sand is transported before high tide due to high mean flows
- Infragravity-wave bores contribute to suspension and transport

Correspondence to:

A. Engelstad,
A.C.Engelstad@uu.nl

Citation:

Engelstad, A., Ruessink, B. G., Hoekstra, P., & van der Vegt, M. (2018). Sand suspension and transport during inundation of a Dutch barrier island. *Journal of Geophysical Research: Earth Surface*, 123, 3292–3307. <https://doi.org/10.1029/2018JF004736>

Received 25 APR 2018

Accepted 22 NOV 2018

Accepted article online 30 NOV 2018

Published online 12 DEC 2018

A. Engelstad¹ , B. G. Ruessink¹ , P. Hoekstra¹ , and M. van der Vegt¹ ¹Department of Physical Geography, Faculty of Geosciences, Utrecht University, Utrecht, the Netherlands

Abstract Overwash and inundation of barrier islands transport large amounts of sediment landward, which could potentially increase the aggradation of these islands in times of sea level rise. However, not much is known about the detailed processes of sediment suspension and transport during inundation. Here we analyze field data of suspended sediment, water levels, waves, and currents which were collected during five inundation events on a barrier island in the Netherlands. We found that depth-integrated suspended sand concentrations and cross-shore sand transport showed high variability during and between inundation events at our location, where 80% of the combined transport from all inundation events was completed before high tide. This is primarily caused by variations in cross-shore flow velocities which were strongest (up to 1.2 m/s onshore) before high tide. However, episodically high depth-integrated suspended sand concentrations (defined as $>2\text{kg/m}^2$) were observed on infragravity time scales ($\sim 20\text{--}200\text{ s}$), suggesting that the contribution of infragravity waves to the combined bed shear stresses of waves and currents was important. High contributions of infragravity waves to the transport coincided with observed bore-like wave shapes, which might partly be attributed to higher short waves riding and suspending sediment at the position of the crest. Two transport regimes were thus found to govern the transport during inundation: a flow-driven regime when flow velocities were high ($>0.5\text{ m/s}$) and the ratio of infragravity wave and current related shields numbers was below 0.11 and an episodic regime when this ratio exceeded 0.11.

1. Introduction

Overwash and inundation of barrier islands can carry large amounts of sediment landward. Overwash is the overtopping of beaches or dune crests, while during inundation the area between ocean and back-barrier basin is continuously submerged (Sallenger Jr, 2000). These processes are commonly forced by elevated water levels resulting from storm surges and wave setup during extreme meteorological events such as storms and hurricanes. The associated morphological responses include erosion and an increase in island instabilities, shoreline retreat, and breaching (Donnelly et al., 2006; Safak et al., 2016), but also sediment accretion such as gains in subaerial areas (Durán et al., 2016). During Hurricane Ivan on 26 September 2004, for example, washovers (the sediment deposits of overwash) of 1.2–1.5 m thickness were deposited on Santa Rosa Island, United States (Donnelly et al., 2006). In fact, overwash can transport up to several hundreds of cubic meters sand per meter beach width landward (Masselink & van Heteren, 2014; Morton & Sallenger, 2003; Nielsen & Nielsen, 2006). Specifically in mesotidal, mixed energy systems, this landward transport can result in net sediment accretion, particularly on the broader and higher barrier islands in the North Sea (Christiansen et al., 2004; Morton & Sallenger, 2003; Nielsen & Nielsen, 2006).

Studies investigating the morphological response to overwash and inundation and the underlying physical processes of sediment suspension and transport focused mostly on presurvey and postsurvey of the affected areas (Matias et al., 2009; Morton & Sallenger, 2003; Nielsen & Nielsen, 2006), laboratory work (Edge et al., 2007; Matias et al., 2013), and numerical modeling (Harter & Figlus, 2017; McCall et al., 2010, 2011; Van Dongeren & Van Ormondt, 2007; Wesselman et al., 2017). Due to the difficulties of collecting field data during storms and hurricanes, onsite studies which combine hydrodynamics and morphological response during overwash and inundation (Fisher et al., 1974; Holland et al., 1991; Hoekstra et al., 2009; Leatherman, 1976; Matias et al., 2010; Sherwood et al., 2014; Van der Vegt & Hoekstra, 2012) are rare. However, field studies are vital to improve insight into sediment transport processes during inundation and will be valuable to validate model studies.

©2018. The Authors.

This is an open access article under the terms of the Creative Commons Attribution-NonCommercial-NoDerivs License, which permits use and distribution in any medium, provided the original work is properly cited, the use is non-commercial and no modifications or adaptations are made.

Models are needed, for example, to assess the risk of barrier island erosion and to estimate the response of barrier islands to sea level rise.

In general, sediment suspension and transport is forced by the mean flow and the orbital motion of short (~ 0.05 – 1 Hz) and infragravity (~ 0.005 – 0.05 Hz) waves, see Aagaard et al. (2013) for an extensive review. During inundation of gently sloping barriers, wave dynamics show similarities with dissipative beaches where incident storm waves break and infragravity waves dominate the inshore wave field. In contrary to a beach situation, however, not all wave energy is eventually dissipated or reflected as short and infragravity waves propagate onshore across the submerged part of the island, and mean flows are predominantly landward directed. The latter are driven by the wave forces induced by breaking waves and pressure gradients. Pressure gradients are caused by the large-scale water level gradient between ocean and back-barrier basin in addition to local wave setup. Large-scale and local pressure gradients can oppose each other at times (Engelstad et al., 2017). Further, higher water levels in the back-barrier basin than on the ocean side were observed to generate seaward flows (Engelstad et al., 2017; Hoekstra et al., 2009; Sherwood et al., 2014), which was also found in modeling studies (Harter & Figlus, 2017; Sherwood et al., 2014; Wesselman et al., 2017). In a combined observation-modeling study of barrier island inundation in the Gulf of Mexico, Sherwood et al. (2014) found that the seaward directed water level gradient resulted in the deposition of a significant amount of sediment on the ocean side. A modeling study by McCall et al. (2010) suggested that higher water levels in the back-barrier relative to the surge levels in the ocean increased back-barrier deposition and reduced deposition in the basin due to a decrease in flow velocity. This is in agreement with simulations by Wesselman et al. (2017) for the Dutch island of Schiermonnikoog. In addition, model results for their study suggested that while currents play a major part in sediment stirring, stirring by incident and infragravity waves was found to be important, too.

The objective of this study is to investigate the respective contribution of mean flows and waves on sand suspension and cross-shore sand transport during barrier island inundation. While we expect the dominant force in sand suspension and transport to be the mean flow, it is of interest to examine the contribution of incident and infragravity waves on sand suspension and transport, especially at times when the magnitude of the mean cross-shore current decreases or even reverses. For this, hydrological and morphological data were collected during a 2-month field campaign on the Dutch island of Schiermonnikoog. Depth-integrated sand concentrations were compared to the forcing by mean flows and waves, while the contributions of incident waves, infragravity waves, and mean currents to the sand transport were analyzed. Field site, instrumentation, initial data processing, and boundary conditions is described in section 2. In section 3, the methodology used to analyze the sand suspension and transport processes are introduced. The results, based on six recorded inundation events, are presented in section 4, followed by a discussion in section 5. Finally, the work is concluded in section 6.

2. Data Collection and Boundary Conditions

2.1. Field Site and Instrumentation

Field data were collected during a 2-month campaign (24 November 2016 to 2 February 2017) on the eastern tip of the Dutch barrier island Schiermonnikoog. Schiermonnikoog is part of a barrier island chain, separating the North Sea and the back-barrier basin, named Wadden Sea (Figure 1). The island is ~ 18 km long and ~ 1.5 km wide at its narrow down-drift eastern end and is aligned at $\sim -10^\circ$ with true East. The system has a tidal range of ~ 1.5 – 2.4 m, and the tidal wave propagates from West to East. Mean offshore significant wave heights range between 0.5 m in summer and 2 m in winter (Oost et al., 2012), while they can typically reach around 7 m during storms. Storm surges can severely increase water levels along the coast and the barrier islands, with the highest recorded water levels reaching ~ 3.5 – 4 m above mean sea level (Hoekstra et al., 2009; Oost et al., 2012).

The instrument transect was placed in an area which is approximately alongshore uniform (Figure 2), but a tidal inlet is located ~ 1.5 km to the east. This area was chosen as a field site because it is open to flooding from the North Sea and the Wadden Sea side, and the low profile (maximum height of the beach crest is ~ 1.7 – 1.8 m above mean sea level) allowed for a higher frequency of inundation compared to other parts of Schiermonnikoog. The field site usually inundates only during northwesterly storms in conjunction with high tide, leaving it subaerial during low tide. Grain sizes at the instrument locations ranged between ~ 100 and 400 μm with a median grain size of ~ 200 μm . Behind the crest, from ~ 300 to 900 m (Figure 3), embryo dunes



Figure 1. Barrier islands are fronting the coasts of The Netherlands and Germany. The Wadden Sea encompasses a series of back-barrier basins between the islands and the coast. The field site (marked by the white line) was located on the eastern tip of the barrier island Schiermonnikoog.

with heights of up to 0.5 m were initially dispersed on the otherwise quite flat surroundings and were covered by sparse vegetation.

To measure flow velocities, waves, water levels, and suspended sand concentrations, instruments were placed roughly cross-shore (Figure 2) across the island tip from the North Sea to the Wadden Sea over a distance of ~ 1.1 km (Figure 3). Four stand-alone pressure sensors (Ocean Sensor System Wave Gauge, type OSS1-010-003C) sampled continuously at 10 Hz with an accuracy of ~ 1 mbar (P1–P4 in Figure 3). Two of the

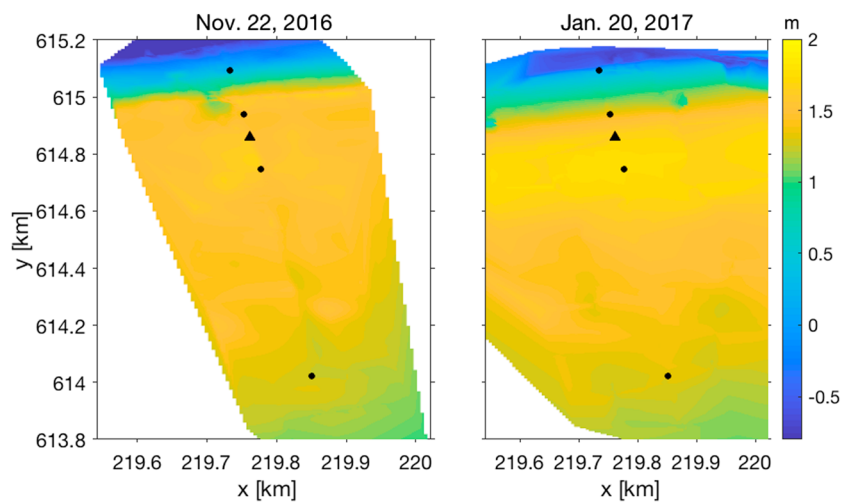


Figure 2. Topography of the field site with bed levels at the beginning of the campaign (left panel) and at the end (right panel). The height is given with respect to Mean Sea Level. Dots mark the stand-alone Ocean Sensor System pressure sensors, while the triangle marks the instrument frame (further described in Figure 3).

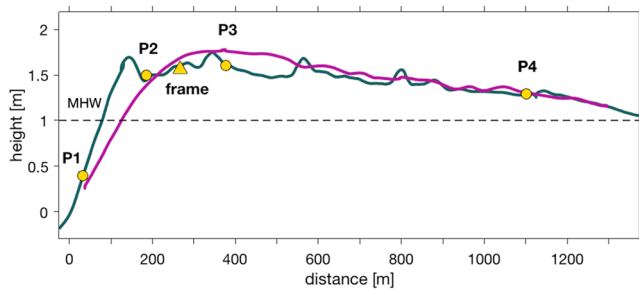


Figure 3. The cross-island profiles at the beginning (gray line) and the end (purple line) of the campaign are shown with the North Sea to the left and the back-barrier area (Wadden Sea) to the right. Yellow dots mark the stand-alone Ocean Sensor System pressure sensors. The yellow triangle marks the instrument frame equipped with Sontek Acoustic Doppler Velocimeter (pressure and currents), Seapoint Turbidity Meters (suspended sediment), and Aquatec Acoustic Backscatter Sensor.

pressure sensors were placed on the beach slope (steepness of 1:80), one after the crest and another one at the Wadden Sea side. An instrument frame, similar to the one deployed by Ruessink (2010), was initially located just behind the beach crest. The location was chosen in an area free of vegetation and embryo dunes such as to not obstruct the flow. It was equipped with a sideways oriented Sontek Acoustic Doppler Velocimeter Ocean (ADVO) probe, sampling at 10 Hz in bursts of 29 min and a break of 1 min. A vertical array of seven Seapoint Turbidity Meters (STM) measuring suspended sand concentrations, and a Pressure Transducer measuring nearbed pressure were added to the frame. Pressure Transducer and STMs sampled at 4 Hz. The frame further contained an Aquatec AQUAscat1000R Acoustic Backscatter Sensor with three transducers (1, 2, and 4 MHz), of which the 1 MHz transducer was used to estimate the distance to the bed, as in Ruessink (2010). The ADVO and Acoustic Backscatter Sensor sampled in the same burst interval and were triggered externally to synchronize measurements. All instruments on the frame collected data only when submerged to save battery power. The initial distance to the bed was 0.16

m for P1 and varied between 0.07 and 0.1 m for P2–P4. The ADVO was located at 0.29 m above the bed, while the initial distance to the bed for the STMs was 0.06, 0.12, 0.18, 0.25, and 0.32 m.

The transect profile and the height of the instrument locations were measured with a Real Time Kinematic Global Positioning System with an accuracy of ~ 0.02 m in the horizontal and ~ 0.03 – 0.05 m in the vertical at the start and end of the campaign.

2.2. Initial Data Processing

All data were processed in 15-min blocks for time series of water levels, wave heights, and velocities. Pressure data were rejected when sensor coverage was less than 0.04 m to avoid intermittent exposure to air. Pressure data were corrected for air pressure and converted to free surface elevation using linear wave theory. The free surface elevation was then low-pass (0.005–0.05 Hz) and high-pass (0.05–1 Hz) filtered, from which infragravity and short wave heights were calculated as four times the standard deviations of the filtered surface elevations. The velocity data were downsampled to 4 Hz to match the sampling rate of the other instruments on the frame and were objected to further quality controls following the guidelines by Elgar et al. (2005) and Mori et al. (2007). If less than 5% of the record did not pass the quality control, the data were interpolated, otherwise the block was rejected. Velocities for locations throughout the water column were calculated by separating the velocities into mean flow, \vec{U}_{mean} , and oscillatory components, $\vec{U}_{osc}(t)$, for each 15-min block and assuming that in the observed shallow water depths the oscillatory components of the velocity were constant throughout the water column. Velocities at depth z were found by using the Karman-Prandtl boundary equation and substituting $\vec{U}_{osc}(t)$ back into the equation

$$\vec{U}_{fit}(t, z) = \frac{\vec{U}_{*c}}{K} \ln\left(\frac{z}{z_0}\right) + \vec{U}_{osc}(t), \quad (1)$$

where \vec{U}_{*c} is the current related shear velocity vector, K is the Van Karman constant (0.41), z is the height of the instrument above the bed, and z_0 is the roughness length calculated from the median grain diameter. \vec{U}_{*c} was found from \vec{U}_{mean} of the single point measurements and in turn was used to estimate the velocities at locations between the bed and the surface. Finally, $\vec{U}_{fit}(t, z)$ was depth-averaged to yield $\vec{u}(t)$. Cross-shore and alongshore velocities account for the island angle.

Instruments were intermittently buried by sand. Burial depths for the pressure sensor P3 were visually estimated from the raw data during times when the instruments were not inundated and measured only air and pore pressure. To account for instrument burial in calculations of sea surface elevations, the correction factor of Raubenheimer et al. (1998) was used. Data presented in this publication can be accessed through Engelstad et al. (2018).

2.3. STM Processing

The STMs were post-calibrated in a recirculation tank with sand samples collected from the bed at the frame location. Background noise in concentration time series was removed as the fifth percentile of each 15-min block (Aagaard & Greenwood, 1994; Brinkkemper et al., 2017; De Bakker et al., 2016), and resulting values

Table 1

Boundary Conditions for Observed Floodings

Flooding #	Date	Wind speed [m/s]	Wind direction [°]	Wave			Water level	
				Hs [m]	T [s]	θ [°]	N. Sea [m]	W. Sea [m]
1	26 December 2016	16	270	6.20	8.7	307	2.34	2.52
2	27 December 2016	11	300	5.11	8.3	327	1.84	2.19
3	04 January 2017	15	310	4.55	7.2	321	2.05	2.16
4	04 January 2017	17	330	6.36	9.2	335	1.89	2.35
5	13 January 2017	20	330	7.43	10.1	326	2.50	2.92

Note. If dates are listed twice, two inundation events occurred on 1 day and were separated by a low tide. Wind speed and direction as well as significant wave height (Hs), periods (T), and wave angle (θ) were measured by an offshore meteorological station (Wierumergronden) and a wave buoy (Schiermonnikoog Noord) and were averaged over 1 hr at high tide. Water levels (wl) in the North Sea (N. Sea, measured at Huibergat) and Wadden Sea (W. Sea, measured at Schiermonnikoog station) were also averaged over one hour at high tide.

$<0 \text{ kg/m}^3$ were set to zero. Substantially higher concentrations at sensors closer to the surface than near the bed suggest the presence of air bubbles. If these were single spikes in the record, the spikes were removed and the gaps were interpolated from adjacent data points. Continuously high values with respect to lower sensors were culled from the data set. If the number of unreliable values exceeded 5% of data points in the block, data from the sensor were discarded for the whole 15-min block. All remaining blocks of sand concentrations were then visually inspected. Records with unreasonably high values, which might have been caused by objects such as, for example, algae, or (partial) burial, were removed. During some inundation events, the bed was highly mobile and varied as much as 0.1 m during a single flooding, causing sensors to be buried or unburied by sand. This led to a varying amount of STMs that could be used for analysis during a single inundation event.

2.4. Hydrodynamic Conditions

The field site was inundated at least eight times during storms in the observational period. Every inundation that was measured is here treated as a single flooding event, even though several floodings might have occurred during a single storm. Here five floodings, during which data covered at least 2 hr, were used for analysis. Wind speeds ranged from 11 to 20 m/s with wind directions from W to NW (Table 1), which were measured at the meteorological station Lauwersoog (Figure 1). Water levels, measured at the tidal stations Huibergat and Schiermonnikoog, exceeded the threshold of the beach crest ($\sim 1.7 \text{ m}$) during these events and were higher in the Wadden Sea compared to the North Sea at high tide (Table 1) and, in fact, for most of the inundation duration. Inundation depths at P2 (Figure 4), which was initially located landward of the crest but was eventually located seaward of the crest, ranged between 0.85 and 1.5 m at high tide.

Offshore significant wave heights, measured at the buoy Schiermonnikoog in approximately 20 m depth, ranged from 4.5 to 7.4 m during inundations with mean wave periods between 7 and 10 s and wave directions

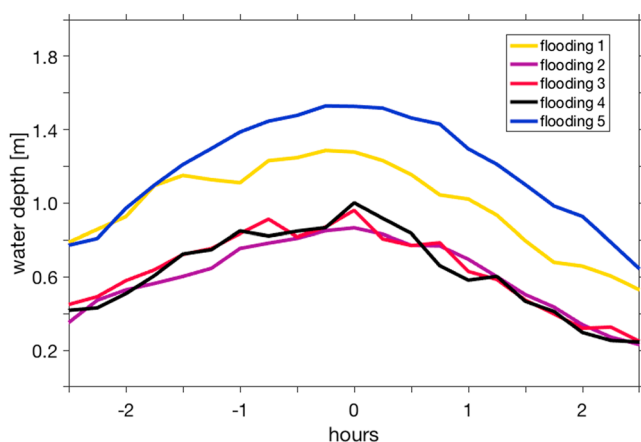


Figure 4. Water depths for all flooding events at P2. The x axis shows the time relative to high tide (0 hr).

from the NW (Table 1). Wind data (Table 1) in addition to offshore wave and waterlevel data are available from Rijkswaterstaat, the Dutch Ministry for Infrastructure and Water Management. Waves had already lost most of their energy seaward of the field site, but short waves continued to break at least until the location of the frame, while infragravity waves appeared to be breaking up to at least m 400 in Figure 3. Short wave heights ranged between 0.3 and 0.65 m (Figure 5b) at the crest. Infragravity wave heights (Figure 5a) were similar to short wave heights and exceeded these during some floodings with low inundation depths (flooding 2 and 4).

Depth-averaged mean cross-island flow velocities ranged from 0 to 1.2 m/s and at times reversed to a seaward flow of max -0.2 m/s (Figure 6a). The cross-shore velocities at the frame were forced by wave breaking seaward of the frame in addition to large-scale and local water level gradients (not shown; Engelstad et al., 2017). While the local water level gradients were partly a function of the large-scale water levels in North and Wadden Sea, they were strongly modified by wave setup. This forced the local gradients

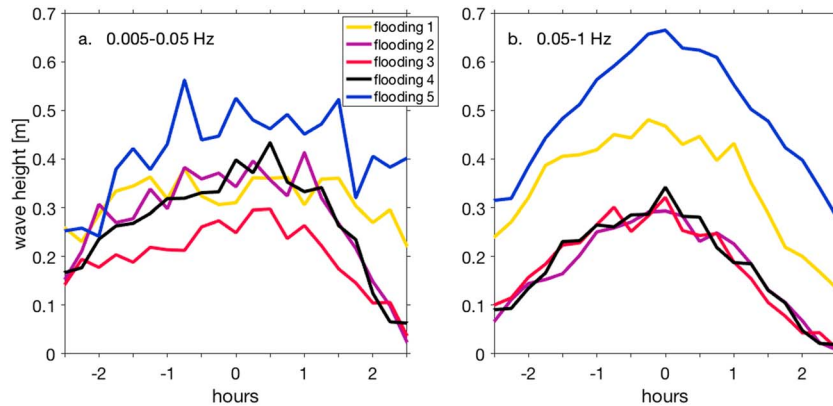


Figure 5. Infragravity (a) and short (b) wave heights for all inundation events at P2. The x axis shows the time relative to high tide (0 hr).

to be landward directed, even though the gradients between North and Wadden Sea were predominately seaward directed even before high tide (inferred from measurements at P1 and P4, not shown).

Depth-averaged mean alongshore velocities (Figure 6b) were of the same magnitude as the cross-shore velocities and even exceeded these at times (e.g., flooding 1 and 5). The high alongshore velocities were probably forced by incident wave angles (inducing pressure and radiation stress variations) and forcing by strong local alongshore winds. Cross-shore and alongshore velocities were markedly reduced after high tide. The reduction in cross-shore velocities can be explained by the falling tide in the North Sea, while longshore velocities might have been reduced by the tidal forcing and/or by a higher water level in the tidal inlet ~1.5 km to the East.

As mentioned, the area was sparsely covered with vegetation and embryo dunes at the beginning of the field campaign. While the embryo dunes were flattened out during the inundation events, most of the vegetation survived. The beach crest transitioned landward during the duration of the field campaign (Figure 3). The beach slope changed from 1:80 (initially) to 1:160 (final), while the highest point of the profile (~1.74 m above mean sea level) was initially located just seaward of P2 but moved landward and was ultimately located at P3 (~1.8 m above mean sea level).

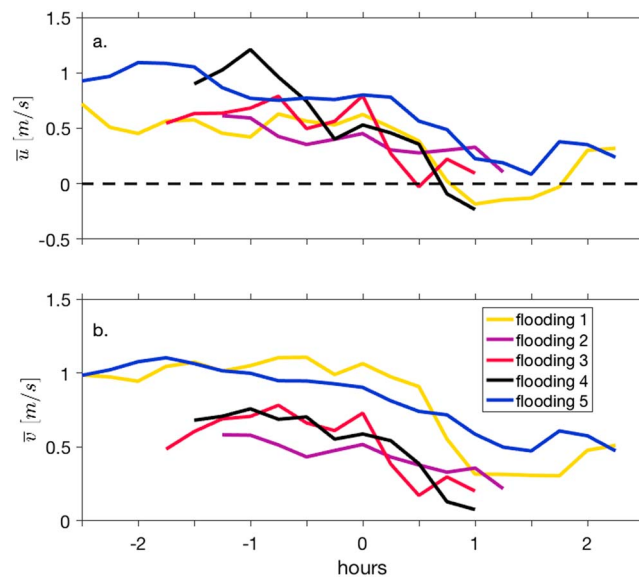


Figure 6. Depth-averaged mean cross-shore, \bar{u} , (a) and alongshore, \bar{v} , (b) velocities at the frame. Positive cross-shore velocities indicate landward flow and positive alongshore velocities are directed to the East. The x axis shows the time relative to high tide (0 hr).

3. Analysis of Sand Suspension and Transport

3.1. Sand Suspension

To account for variations in STM height above the bed with time which can introduce large variations in measured sand concentrations, the varying amount of STMs, and to obtain estimates of the net suspended sand loads throughout the water column, the available concentrations were depth-integrated. For this, the vertical concentrations were linearly fitted to estimate concentrations from bottom to surface, so that instantaneous depth-integrated suspended sediment concentrations, $c(t)$, were calculated from

$$c(t) = \int_0^d C_{fit}(t, z) dz, \quad (2)$$

where $C_{fit}(z, t)$ are the concentrations estimated from the linear fit. These were integrated from the bed ($z = 0$) to the top of the water column ($z = d$). Time averages of the depth-integrated concentrations will be denoted as C .

We acknowledge that a linear fit might be an oversimplification and that real values could be higher due to an increase in suspended sediment concentrations close to the bed. In other words, the linear approach results in a conservative estimate of the sand concentrations which can be regarded as a lower error bound. Using an exponential fit on instantaneous field data is difficult. Greater distances from the bed (>0.15 m), intermittently low (close to zero) instantaneous values for higher sensors, or higher values for higher sensors compared to the lowest sensor all can result in unreasonable high instantaneous concentrations ($>10^4$ kg/m³), leading to serious overpredictions. The use of time-averaged (15 min) concentrations at each sensor allowed to estimate mean concentrations with an exponential fit, here used as an upper error bound for the difference between the two approaches. While the difference between the two fits is small if only two sensors are available (transport based on the exponential fit is ~ 1.1 times greater than for the linear fit), the difference is greater for more sensors (on average the exponential fit is 1.5 times greater than the linear fit, in one case up to 2.5 times). We could not detect a consistent bias by using the linear fit in the analysis, since the difference between the two fits varied for time and for floodings. Differences in the volume transport estimates between lower (linear fit) and upper (exponential fit) bounds will be discussed in section 5.2).

The suspension mechanisms can be evaluated using the Shields parameter

$$\theta = \frac{\tau}{(\rho_s - \rho_w)gd_{50}}, \quad (3)$$

where ρ_s (here taken as 2,650 kg/m³) and ρ_w (1,025 kg/m³) are the sediment and water densities, respectively, g is the gravitational acceleration (9.81 m/s²), and d_{50} is the medium grain size (203 μ m). The Shields parameters related to the mean currents, θ_c , and waves, θ_w , are dependent on the corresponding bed shear stresses τ_c (currents) and τ_w (waves) which are described below following Van Rijn (1993):

$$\tau_c = \frac{\rho_w g |\bar{U}_{fit}|^2}{C_z^2}, \quad (4)$$

with C_z being the Chézy coefficient for smooth turbulent flow conditions and the overbar indicates time averages. \bar{U}_{fit} is used to account for the fact that alongshore velocities were of the same order as cross-shore velocities and contributed to the bed shear stresses. The Chézy coefficient is

$$C_z = 5.75g^{0.5} \log_{10} \left(\frac{12d}{\alpha d_{90} + 3.3 \frac{\nu}{|\bar{U}_*|}} \right). \quad (5)$$

Here α was set to 2, d_{90} is the grain diameter representing the 90% cumulative percentile value, ν is the kinematic viscosity coefficient, and $|\bar{U}_*|$ is the magnitude of the bed shear velocity. Instantaneous Shields parameters, $\theta_i(t)$, were calculated with equations (4) and (5) by using instantaneous velocities. The bed shear stress due to the wave motion, τ_w , is estimated as

$$\tau_w = 0.25 \rho_w f_w U_{osc}^2, \quad (6)$$

where the wave related friction coefficient, f_w , is defined as

$$f_w = 0.09 \left(\frac{U_w A_w}{\nu} \right)^{-0.2}, \quad (7)$$

which gives similar results as the wave friction factor defined by Swart (1974). The fluid particle excursion, A_w , is described by

$$A_w = \frac{T_p}{2\pi} U_w, \quad (8)$$

where T_p is the peak wave period and the peak orbital velocity, U_w , is defined as

$$U_w = \pi \frac{H_s}{T_p \sinh(kd)}, \quad (9)$$

with H_s being the total significant wave height, which is used here in the limit 0.005–1 Hz to account for the importance of short as well as infragravity waves, and k the wave number. θ_w was further separated into the Shields parameter for short, θ_{short} , and infragravity, θ_{ig} , waves by applying equation (3) to the short and infragravity wave contributions. The critical Shields parameter for suspension, $\theta_{cr, suspension}$, was found to be 0.08 for the present sediment, following Van Rijn (1993). Varying α and ν or using the parametrization for rough turbulent flow conditions altered θ slightly (± 5 –10%), but did not change the general findings.

3.2. Sand Transport

The instantaneous depth-integrated suspended sand transport rate, $\vec{q}(t)$, is given by

$$\vec{q}(t) = \int_0^d \vec{U}_{fit}(t, z) C_{fit}(t, z) dz, \quad (10)$$

and the net, time-averaged and depth-integrated, suspended sand transport rate is computed as

$$\vec{Q} = \frac{1}{T_b} \int_0^{T_b} \int_0^d \vec{U}_{fit}(t, z) C_{fit}(t, z) dz dt, \quad (11)$$

where T_b is the block duration (15 min). To investigate the contributions of waves and mean flow to the suspended cross-shore sand transport, Q_u , the cross-shore component of \vec{Q} , Q_u , can be separated (Jaffe et al., 1984) into the mean (Q_c) and oscillatory, wave transport (Q_w).

$$Q_u = Q_c + Q_w = \int_0^d \overline{U}_{fit}(z) \overline{C}_{fit}(z) dz + \frac{1}{T_b} \int_0^{T_b} \int_0^d U_{osc}(t, z) \tilde{C}_{fit}(t, z) dt dz, \quad (12)$$

where U_{fit} is the instantaneous cross-shore velocity (estimated by equation (1)), overbars indicate mean and tildes oscillating components. The transport by waves was computed from the cospectrum (the real part of the cross-spectrum) of velocity $U_{fit}(t, z)$ and suspended sediment concentrations $C_{fit}(t, z)$ (Huntley & Hanes, 1987) at each height z . Due to the almost equal importance of short and infragravity waves (Figure 5), the wave transport was further subdivided into the short (0.05–1 Hz) and infragravity (0.005–0.05 Hz) range to investigate their respective contributions. The time-averaged and depth-integrated transport by infragravity waves is denoted as Q_{ig} and by short waves as Q_{short} . We assume that Q_c not only implicitly includes sand suspension by the flow, but that it can include sand brought into suspension by infragravity and short waves, while Q_{ig} can include sand brought into suspension by the short waves if short wave heights were not equally distributed during the onshore and offshore stroke. At the same time, Q_{short} could potentially include sand suspended by infragravity waves and the flow in addition to short wave suspension, albeit this contribution is assumed to be small and only effective for nonlinear short waves. The relative contribution of mean flow, infragravity, and short waves to the time-averaged sand transport is found by dividing the respective value by the sum of all absolute contributions ($Q_{all} = |Q_c| + |Q_{ig}| + |Q_{short}|$).

4. Results

4.1. Suspended Sand Concentrations

Estimated time-averaged and depth-integrated suspended sand concentrations, C , varied significantly during each individual flooding, as well as between flooding events (Figure 7a). C were usually highest at the onset

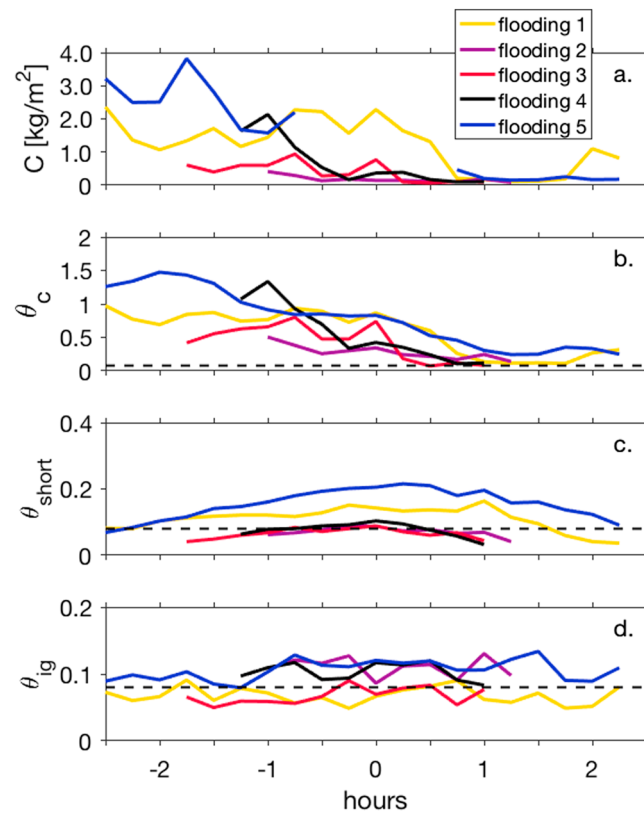


Figure 7. Depth-integrated, time-averaged suspended sediment concentrations (a) compared to depth-averaged current, θ_c , (b) short-wave, θ_{short} , (c) and infragravity, θ_{ig} , (d) Shields parameters. The black dashed line shows the critical Shields parameter for suspension, $\theta_{cr,suspension}=0.08$. The x axis shows the time relative to high tide (0 hr). Values for flooding 5 around high tide in (a) are missing since Seapoint Turbidity Meters were buried. Note the different vertical scales for θ_c , θ_{short} , and θ_{ig} .

of inundation ($0.4\text{--}3.8\text{ kg/m}^2$) and dropped considerably for most flooding events after high tide (Figure 7a), but minimum values still reached $\sim 0.1\text{ kg/m}^2$.

Sand suspension appears to be foremost driven by the current related bed shear stresses (compare Figures 7a and 7b), here expressed by the nondimensional Shields parameters, θ_c (see section 3.2). The current related Shields parameters, θ_c , were highest (max of 1.5 during flooding 5) at the onset of floodings due to high mean flows (Figure 6). They continuously exceeded the critical Shields number for sand suspension, $\theta_{cr,suspension}$, of ~ 0.08 , and were >0.25 during all floodings before high tide. Wave related Shields parameters were comparably lower, with a maximum of ~ 0.2 for short and ~ 0.13 for infragravity wave Shields parameters. While θ_{short} exceeded $\theta_{cr,suspension}$ for all floodings during high tide, they were highest for short waves exceeding 0.3 m. θ_{ig} for flooding 1 and 3 fluctuated around $\theta_{cr,suspension}$, suggesting that here the infragravity waves contributed less to the sand suspension, owing to either low infragravity wave heights (flooding 3, Figure 5a) or larger inundation depths (flooding 1, Figure 4).

Time-series of sand suspension show an episodic nature of sand suspension (Figures 8 and 9). A comparison of instantaneous depth-integrated concentrations, $c(t)$, depth-averaged cross-shore velocities, $u(t)$, and Shields parameters, θ_i , indicate that the suspension of sediment was partly driven by short waves (see e.g., the strong, short-period fluctuations in Figure 8, left column). Moreover, higher concentrations (here defined as $>2\text{ kg/m}^2$) were observed particularly at infragravity timescales (Figures 8d, 9a, and 9d) during which sand usually stayed in suspension. Suspension events in correlation with infragravity bores showed sudden high instantaneous values of up to 9.5 kg/m^2 which coincided with the crest of bores where Shields numbers were highest. At times, short waves contributed to these high Shields numbers, since depth modulation by the free infragravity waves allow larger short waves to ride on the crest of infragravity waves, while smaller short waves are positioned in the trough. Thus, short waves are enhancing the suspended concentrations under

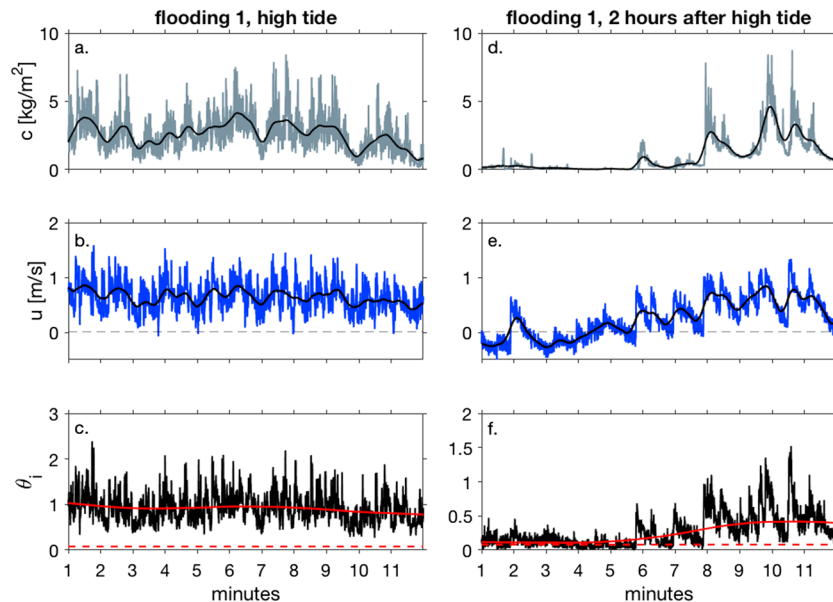


Figure 8. Instantaneous depth-integrated suspended sediment concentrations (a and d), compared to depth-averaged cross-shore velocities (b and e) and Shields parameters (c and f) shown for flooding 1 at high tide (left column) and at the end of the flooding (right column). The solid black lines shows the low-pass (0.005–0.05 Hz) filtered suspended sediment concentrations (c and d) and cross-shore velocities (b and e). The red dashed line in (f) indicates the critical Shields parameter, $\theta_{cr,suspension} = 0.08$, and the red solid line shows the running mean (4-min window). Note the different vertical scales for θ_{uv} in (c) and (f).

infragravity wave crest further as described previously by De Bakker et al. (2016). Generally, infragravity waves appear to modulate the shear stress of the mean flow (here estimated by a running mean with a 4 min window, shown as a red solid curve in Figures 8 and 9) by enhancing it if the stroke is in the same direction as the mean flow (for example, during the onshore infragravity wave stroke, compare Figures 9b and 9c, or the offshore stroke, compare Figures 9e and 9f) or by reducing it if the stroke is in opposite directions. At times of low or offshore-directed mean velocities, infragravity bores and short waves were not able to mobilize the very high concentrations seen in the presence of high mean flow velocities (see e.g., minute 1 in Figures 8d–8f and minutes 5–11 in Figures 9d–9f). During the mean flow reversal, when short and infragravity waves were of about the same magnitude as an hour before high tide, the Shields parameter repeatedly dropped below the critical value for suspension and sand suspension was at a minimum (Figure 9, compare left and right panel). This suggests that the combined components of episodically high wave velocities and mean flow caused the high suspended concentrations.

4.2. Sand Transport

The total, mean depth-integrated, cross-shore sand transport rate, Q_{uv} , was highest at the start of inundations with a maximum of $\sim 3.8 \text{ kg}\cdot\text{m}^{-1}\cdot\text{s}^{-1}$ for flooding 5 and decreased significantly around and after high tide to values of $\sim 0.05 \text{ kg}\cdot\text{m}^{-1}\cdot\text{s}^{-1}$ (Figure 10). In fact, $\sim 80\%$ of the combined transport from all floodings was done before high tide. Not surprisingly, the sand transport was highest for flooding events with high mean flow velocities, such as floodings 1, 4, and 5, and the net transport followed the suspended sand concentrations closely (compare Figures 7a and 10). The net, depth-integrated, alongshore sand transport, Q_{vw} , was similar or even higher (flooding 1) than Q_{uv} due to the strong alongshore velocities (Figure 6). The direction of the depth-integrated total sand transport was almost entirely directed landward and toward the East (Figure 10). Mean offshore transport was only observed during flow reversal at times when the suspended sand concentrations and seaward directed velocities were low, so that the transport rate was rather small (maximum seaward transport was $0.03 \text{ kg}\cdot\text{m}^{-1}\cdot\text{s}^{-1}$).

Overall, the total sand transport was dominated by the mean flow transport, Q_{cr} (Figure 11) before high tide, which reached a maximum relative contribution of 0.98 during flooding 5. Contributions by infragravity waves, Q_{ig} , increased to > 0.2 when mean flow velocities were roughly $< 0.5 \text{ m/s}$ and reached maximum values of ~ 0.8 during flooding 1 and 2 after high tide. The infragravity transport was generally onshore directed

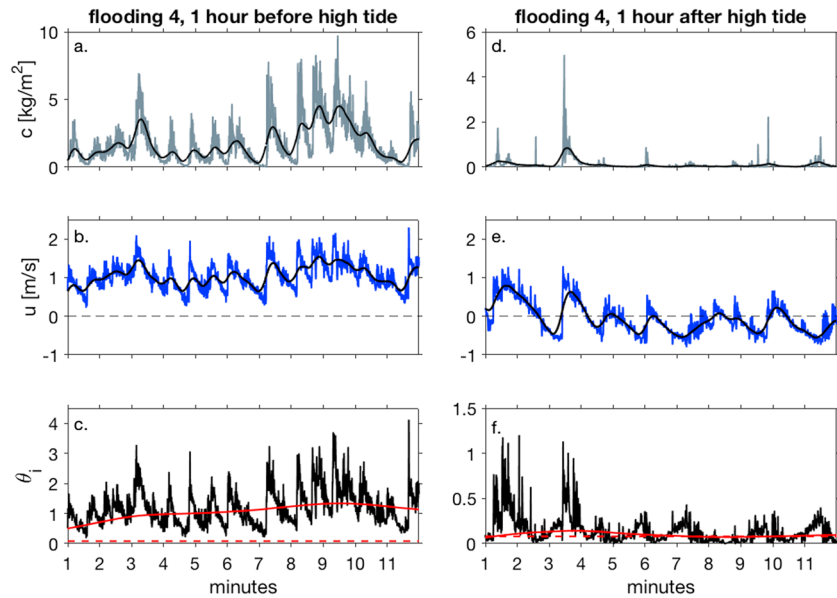


Figure 9. Instantaneous depth-integrated suspended sediment concentrations (a and d), compared to depth-averaged cross-shore velocities (b and e) and shields parameters (c and f) for flooding 4 at the start (left column) and the end of the flooding (right column). The solid black lines show the low-pass (0.005–0.05 Hz) filtered suspended sediment concentrations (c and d) and cross-shore velocities (b and e). The red dashed line in (f) shows the critical Shields parameter, $\theta_{cr,suspension}=0.08$, and the red solid line shows the running mean (4-min window). Note the different vertical scales.

(2% of it was offshore directed). Contributions by short waves, Q_{short} , to the mean cross-shore transport were overall insignificant before high tide (between ~ 0.001 – 0.03) and increased somewhat after high tide (to a maximum of 0.17). (However, while short wave transport was small, short waves contributed to sand suspension.) When the mean flow was seaward directed, the transport by mean flow and infragravity waves opposed each other with the exception of one occasion during flooding 1 when the mean infragravity transport was

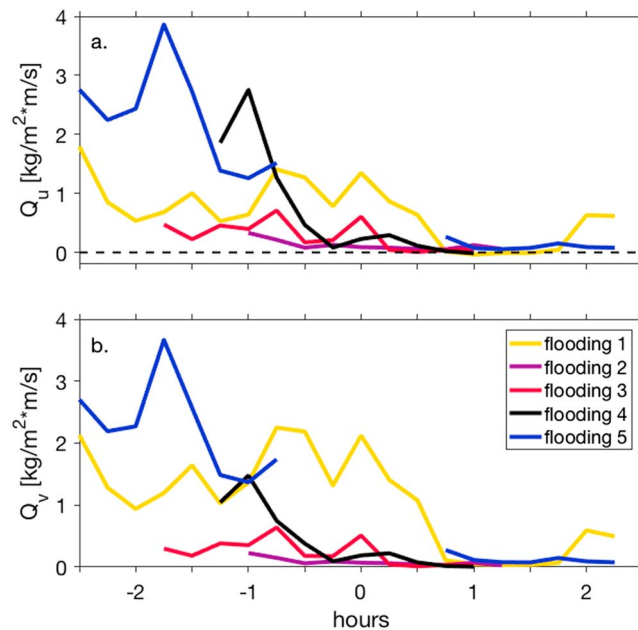


Figure 10. The net, depth-integrated sand transport in the cross-shore, (Q_u), (a) and alongshore, (Q_v), (b) direction. Positive cross-shore is landward, while positive alongshore is approximately toward the East. The x axis shows the time relative to high tide (0 hr). Values for flooding 5 around high tide are missing since STMs were buried.

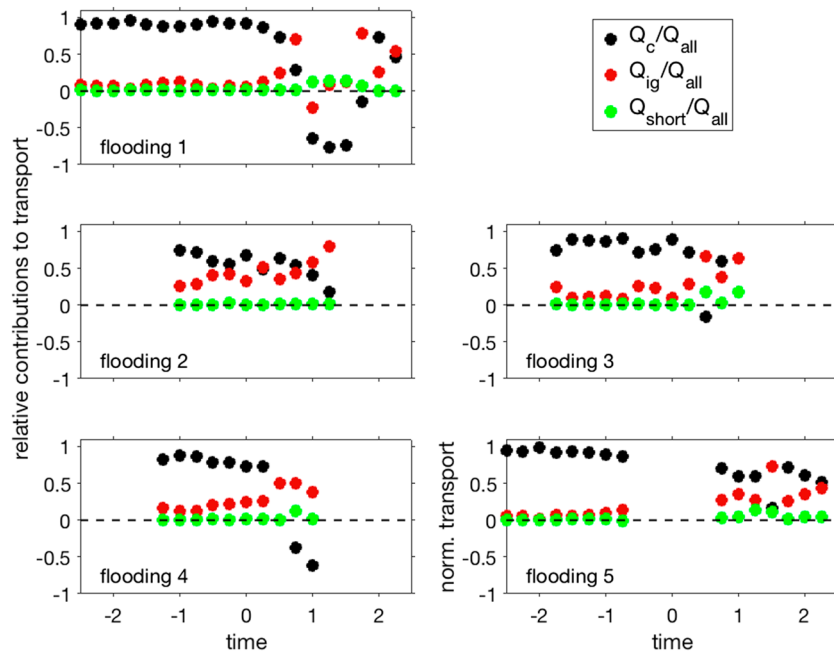


Figure 11. The relative contribution of mean flow, Q_c/Q_{all} , (black dots), infragravity, Q_{ig}/Q_{all} , (red dots) and short, Q_{short}/Q_{all} , (green dots) waves. Positive transport is landward, while negative transport is seaward directed. The x axis shows the time relative to high tide (0 hr). Values for flooding 5 around high tide are missing since STMs were buried.

also offshore directed. This instant of offshore-directed infragravity transport was most likely caused by the fact that the infragravity waves had not developed into a bore-like shape (due to relative deep inundation depths) and short waves were distributed evenly on crests and troughs (not shown). Since in this situation the wave suspension is (more or less) the same under crests and troughs, the mean offshore flow can enhance the offshore-directed transport during the negative infragravity wave phase (De Bakker et al., 2016). On the other hand, when the mean flow was offshore directed during flooding 4, infragravity-bore shapes had developed with larger short waves riding on the crest than in the troughs, causing the transport to be onshore.

4.3. Episodicity of Sand Transport

Results in sections 4.1 and 4.2 suggest that sand transport at the field site was governed by two “regimes.” During high mean flows, suspension and transport were largely driven by the mean flow resulting in an almost continuous transport. In low mean-flow conditions the importance of infragravity waves for sand suspension and transport increased and caused episodic transport. To further distinguish between flow-driven and episodic events (on an infragravity scale), we investigated the episodicity of sand transport. For this, the normalized cumulative transport is used since it highlights the importance of infragravity waves in sand transport.

The cumulative depth-integrated sand transport, Q_{cum} , was calculated for every 15-min block by the cumulative sum of the instantaneous depth-integrated cross-shore transport, q_{tr} , which was then normalized by the (absolute) maximum in cumulative transport for each block, yielding $Q_{cum}/Q_{cum-max}$. Flow-driven events are visually assessed for each block, and are here defined as $Q_{cum}/Q_{cum-max}$ showing a continuous increase in transport over time on time scales longer than 200 s (infragravity time scale) at least once in one block, while episodic events show sudden increases followed by a flat where the increase in $Q_{cum}/Q_{cum-max}$ is close to zero, indicating that transport by mean flow alone is very small or zero.

Flow-driven events, such as floodings 1 and 5 at the onset of the inundation and floodings 1 and 3 during high tide (Figures 12a and 12b), were characterized by high mean flows (>0.5 m/s, Figure 6) and high current bed shear stresses ($\theta_c > 0.5$, Figure 7), while the bed shear stresses caused by infragravity waves were small ($\theta_{ig} < 0.1$). Episodic events, such as flooding 2 during all times or flooding 3 at the start of the inundation, can be observed when $\theta_c < 0.5$ even if θ_{ig} (and θ_{short}) were < 0.1 as for flooding 3 at the start of the inundation. In fact, computations of θ_{ig}/θ_c for all time steps showed that episodic events occurred for θ_{ig}/θ_c above 0.11 (not shown).

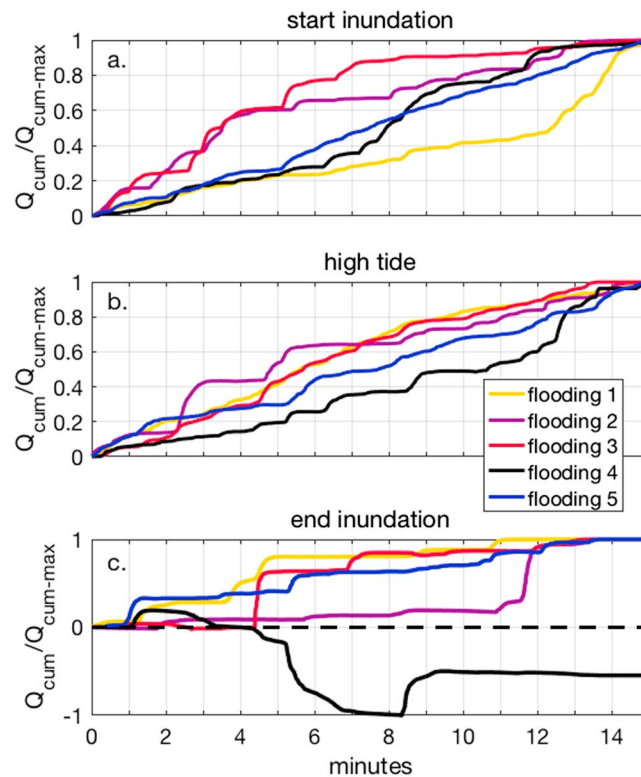


Figure 12. The cumulative depth-averaged sediment transport at the beginning and end of each individual inundation (a and c) and at high tide (b) for 15 min normalized by the maximum of the absolute cumulative transport for the 15 min block. The beginning and end of each flooding relative to high tide can be seen in Figure 10.

The episodic nature of the sand transport increased toward the end of all floodings, when the steps got steeper and the flat plateaus longer (Figure 12c) due to low cross-shore mean velocities. The exception is flooding 4 during which the flow reversed. Here the episodic reduction of the seaward directed transport (expressed in less negative numbers than in the time before) suggest that landward directed infragravity transport reduced the net seaward transport, as was already suggested in section 4.2. Visual inspection of $Q_{cum}/Q_{cum-max}$ for every time step, and ignoring times of (mean flow and infragravity) transport reversal, suggest that for all investigated floodings only about half of the time the transport is dominated by the flow.

5. Discussion

5.1. Profile Change and Sand Transport

Observations showed that during our field campaign the beach and beach crest were eroded, while sand was accumulated landward of the crest. In order to determine how much of the total profile change can be explained by the suspended cross-shore sand transport, the profile change was estimated from the dGPS surveys along the instrument array which were done at the beginning and end of the field campaign. The net volume change along the transect was estimated by the difference in height and integrated along the length of the transect and is given per 1 m width. To establish the change landward of the measurement frame, the change in height was integrated between the instrument frame and the Wadden Sea. We assume that all positive changes landward of the frame must have come from sediment being transported from the seaward side of the instrument frame, and we assume no gradient in the alongshore transport in our region. The net total change (increase) in volume between North and Wadden Sea was $\sim 2 \text{ m}^3/\text{m}$ over the whole observational period, suggesting that the net addition of sediment to the beach from the North Sea is small during winter storms. Between the instrument frame and the Wadden Sea the volume increased by roughly $60 \text{ m}^3/\text{m}$, while the area between North Sea and frame lost $\sim 58 \text{ m}^3$. Volume changes at the Wadden Sea side were negligible and suggest that no sediment was deposited in the Wadden Sea.

The volume of the net cross-shore sand transport across the crest was estimated by the time-integration of the instantaneous sand transport rate, q_{ur} , over the duration of all flooding events and by including two

floodings for which the STMs were intermittently located high (>0.2 m) in the water column. For these the transport is probably underestimated, but can be used for a rough estimate of the total sand transport. Missing values for flooding 5 were replaced by results from flooding 1, assuming them to be the lower limit for flooding 5 transport. The density of dry sand was taken to be $1,600 \text{ kg/m}^3$ with a porosity of 0.4. Adding the sand transport for all events results in a volume transport of $\sim 32 \text{ m}^3/\text{m}$, which is roughly half of the observed change. Part of the underestimation is surely due to the conservative estimate of sand concentrations with the linear fit, which ignores substantially higher concentrations close to the bed. As a comparison, when Q_c , the mean flow transport, was estimated with a linear fit it resulted in roughly 25 m^3 , while the exponential fit, which we view as an upper bound (Section 3.1), yielded $\sim 39 \text{ m}^3$. Since about 80% of the volume is transported by the mean flow, waves would add $\sim 10 \text{ m}^3$ so that the total volume transport for an exponential fit would be around 48 m^3 . This shows that there is a relatively high uncertainty for a long record of sand concentrations measured in the field.

In addition, bedload transport and sheet flow could not be measured, but might have contributed to the transport (Harter & Figlus, 2017). Further underestimations of the cross-shore transport could stem from the fact that nine short inundation events are not included in the calculation, since these were too short or shallow (≤ 0.4 m) to get reliable estimates for the sand transport. These small inundation events will probably not have added much to the overall change. Further, sand transport during the overwash phase, which precedes and follows inundations, is assumed small and in all likelihood less than 1% of the net transport during inundation (Wesselman et al., 2017). However, due to the elevation of the mounted ADV, measurements only started when inundation depths exceeded ~ 0.4 m, so that we might have missed some potentially high values, especially at the onset of inundations. Imprecision in the calculation of the volume change might have been caused by inaccuracies in the dGPS measurements. Another reason for the imbalance between volume change and sand transport could be that the alongshore transport did converge due to increased water levels in the channel located to the east of our field site and contributed to the changes in the area after all. In addition, eolian transport might have contributed to the volume change. Despite these various additional transport processes and the general difficulties of measuring suspended sediment concentrations in a stormy environment, we were able to account for half of the observed volume change.

5.2. Comparison With Other Transport Studies

Generally, the observed erosion and the landward transport of beach and beach crest during inundation agrees well with findings of dune erosion and transport to the back-barrier part of the island during inundation by McCall et al. (2010) and Harter and Figlus (2017). While the seaward sediment transport observed and modeled in previous studies (Goff et al., 2010; Harter & Figlus, 2017; Sherwood et al., 2014; Wesselman et al., 2017), caused by higher water levels in the back-barrier basin than on the ocean side, was also observed in this study, the total observed seaward sand transport is negligible since it adds up to $\sim 0.05 \text{ m}^3$ entirely. Research by Sherwood et al. (2014) and Harter and Figlus (2017) found erosion and scour channels, driven by the seaward flow in the ebbing storm surge, which were not observed at our field location. In addition, their model simulations suggested significant seaward sediment transport and ocean side deposition. Seaward sediment deposition was also observed by Goff et al. (2010). Most of the mentioned research was done in hurricane conditions on low-lying narrow barrier islands and spits, where the strong seaward flow caused by the storm surge ebb after the passing of hurricanes may explain some of the differences in seaward sediment transport. Wesselman et al. (2017) modeled the cross-shore sediment transport at our field location (also at the beach crest). For this, they created water levels and wave conditions (wave heights, periods) from historic data sets and separated them by classes. These were based on the peak water levels in the North Sea, with increasing water levels and wave heights per class. Flooding 5, which had the highest water level (Table 1), corresponds to their class 5 which is defined for North Sea water levels between 2.50 and 2.75 m. While the observed pattern of high landward sand transport at the start of inundations, low transport around high tide, and seaward transport agree qualitatively, the modeled landward transport was $\sim 80\%$ lower than what we observed and the modeled seaward transport of $\sim -0.4 \text{ kg}\cdot\text{m}^{-1}\cdot\text{s}^{-1}$ for class 5 was not observed for flooding 5. This is a result of lower modeled (~ 0.7 m/s) onshore velocities and the modeled seaward velocities of ~ 0.6 m/s, which not only forced the seaward sand transport but also increased sand suspension considerably after high tide. The likely cause for this discrepancy could be that for class 5 the model was forced with offshore significant wave heights of 5.38 m, while observed offshore significant wave heights for flooding 5 were significantly larger (7.43 m). Generally, in equal (shallow) water depths an increase in wave height forces an increase in water level setup which for our field site is located at the crest. This, in turn, increases cross-shore velocities

in the case that the large-scale water level gradient between North- and Wadden Sea is directed toward the Wadden Sea. In cases where the large-scale gradient is directed seaward, setup can counteract the seaward directed velocities or even overcome the large-scale water level gradient altogether so that the flow is still landward directed. This suggests that the sand transport at our field site is not only affected by the large-scale water levels, but also by the offshore wave heights.

6. Conclusions

To improve our understanding of suspended sediment transport processes during inundation, observations of suspended sand concentrations, flow velocities, waves, and water levels were collected during several inundation events on a barrier island in the North Sea during a 2-month campaign. Sand suspension and cross-shore transport showed high variabilities and were highest at the onset of inundations while they decreased considerably after high tide. About 80% of the combined transport from all floodings was done before high tide. This is mainly caused by the difference in mean flow velocities, which on a large scale were determined by water levels in the North and Wadden Sea and on a smaller scale by wave breaking. While suspended sand concentrations were primarily forced by the mean flow, time series of sand concentrations suggest that episodically high depth-integrated suspended sand concentrations (defined as $>2 \text{ kg/m}^2$) were generated by the combined bed shear stresses of infragravity waves, short waves, and currents. High suspension events on infragravity time scales were oftentimes supported by large short waves riding on the crest of infragravity waves, while smaller short waves rode in the troughs. The maximum relative contribution of the mean flow to the total transport, Q_c/Q_{all} , reached 0.98 before high tide, while the maximum contribution of the infragravity waves, Q_{ig}/Q_{all} , reached 0.8 toward the end of inundation events. These observations suggest the existence of two sand transport regimes at our field site: flow-driven regimes which were characterized by high mean flows ($>0.5 \text{ m/s}$) and high current bed shear stresses ($\theta_c > 0.5$) while bed shear stresses generated by infragravity waves were small ($\theta_{ig} < 0.1$), and episodic regimes which can be observed when $\theta_c < 0.5$ and the ratio of infragravity wave and current related Shields numbers $\theta_{ig}/\theta_c > 0.11$. About half of all 15-min time steps were episodic events, highlighting the importance of infragravity waves.

References

- Aagaard, T., & Greenwood, B. (1994). Suspended sediment transport and the role of infragravity waves in a barred surf zone. *Marine Geology*, *118*, 23–48.
- Aagaard, T., Greenwood, B., & Hughes, M. (2013). Sediment transport on dissipative, intermediate and reflective beaches. *Earth-Science Reviews*, *124*, 32–50. <https://doi.org/10.1016/j.earscirev.2013.05.002>
- Brinkkemper, J. A., de Bakker, A. T. M., & Ruessink, B. G. (2017). Intrawave sand suspension in the shoaling and surf zone of a field-scale laboratory beach. *Journal of Geophysical Research: Earth Surface*, *122*, 356–370. <https://doi.org/10.1002/2016JF004061>
- Christiansen, C., Aagaard, T., Bartholdy, J., Christiansen, M., Nielsen, J., Nielsen, N., et al. (2004). Total sediment budget of a transgressive barrier-spit, Skallingen, SW Denmark: A review. *Geografisk Tidsskrift-Danish Journal of Geography*, *104*(1), 107–126. <https://doi.org/10.1080/00167223.2004.10649508>
- De Bakker, A. T. M., Brinkkemper, J. A., van der Steen, F., Tissier, M. F. S., & Ruessink, B. G. (2016). Cross-shore sand transport by infragravity waves as a function of beach steepness. *Journal of Geophysical Research: Earth Surface*, *121*, 1786–1799. <https://doi.org/10.1002/2016JF003878>
- Donnelly, C., Kraus, N., & Larson, M. (2006). State of knowledge on measurement and modeling of coastal overwash. *Journal of Coastal Research*, *22*, 965–991. <https://doi.org/10.2112/04-0431.1>
- Durán, R., Guillá'n, J., Ruiz, A., Jimáñez, J. A., & Sagristá, E. (2016). Morphological changes, beach inundation and overwash caused by an extreme storm on a low-lying embayed beach bounded by a dune system (NW Mediterranean). *Geomorphology*, *274*(Supplement C), 129–142. <https://doi.org/10.1016/j.geomorph.2016.09.012>
- Edge, B. L., Park, Y. H., & Overton, M. (2007). Experimental study of overwash. *Proceedings Coastal Sediments*, *7*, 2074–2083. [https://doi.org/10.1061/40926\(239\)163](https://doi.org/10.1061/40926(239)163)
- Elgar, S., Raubenheimer, B., & Guza, R. T. (2005). Quality control of acoustic Doppler velocimeter data in the surfzone. *Measurement Science and Technology*, *16*(10), 1889. <https://doi.org/10.1088/0957-0233/16/10/002>
- Engelstad, A., Ruessink, B., Hoekstra, P., & van der Vegt, M. (2018). Observational data set: Sand suspension and transport during barrier island inundation. <https://doi.org/10.5281/zenodo.1228517>
- Engelstad, A., Ruessink, B., Wesselman, D., Hoekstra, P., Oost, A., & van der Vegt, M. (2017). Observations of waves and currents during barrier island inundation. *Journal of Geophysical Research: Oceans*, *122*, 3152–3169. <https://doi.org/10.1002/2016JC012545>
- Fisher, J. S., Leatherman, S. P., & Perry, F. C. (1974). Overwash processes on Assateague Island. In *Proceedings of 14th Conference on Coastal Engineering*, ASCE Copenhagen, Denmark, pp. 1194–1211. <https://doi.org/10.1061/9780872621138.073>
- Goff, J. A., Allison, M. A., & Gulick, S. P. S. (2010). Offshore transport of sediment during cyclonic storms: Hurricane Ike (2008), Texas Gulf Coast, USA. *Geology*, *38*(4), 351–354. <https://doi.org/10.1130/G30632.1>
- Harter, C., & Figlus, J. (2017). Numerical modeling of the morphodynamic response of a low-lying barrier island beach and foredune system inundated during Hurricane Ike using XBeach and CSHORE. *Coastal Engineering*, *120*, 64–74. <https://doi.org/10.1016/j.coastaleng.2016.11.005>
- Hoekstra, P., ten Haaf, M., Buijs, P., Oost, A., Klein Breteler, R., van der Giessen, K., & van der Vegt, M. (2009). Washover development on mixed-energy, mesotidal barrier island systems. In M. Mizuguchi & S. Sato (Eds.), *Coastal Dynamics* (Vol. 83, pp. 25–32). Singapore: World Scientific.

Acknowledgments

We thank Marcel van Maarseveen, Henk Markies, and Arjan van Eijk for their excellent technical support without which this work could not have been done. Thanks also go to Daan Wesselman for his support during the field work and discussions afterward. We are grateful for the constructive comments made by two anonymous reviewers and Associate Editor Curt Storlazzi. Natuurmonumenten assisted us during the field work. This work is supported by the Netherlands Organisation for Scientific Research (NWO) under contract 850.13.051, as well as by Natuurmonumenten, the National Forest Service (Staatsbosbeheer, SBB), and the Wadden Academy. The observational data are available from Engelstad et al. (2018).

- Holland, K. T., Holman, R. A., & Sallenger, A. H. (1991). Estimation of overwash bore velocities using video techniques, *Coastal sediments: ASCE*, pp. 489–497. <https://doi.org/10.5670/oceanog.1993.02>
- Huntley, D. A., & Hanes, D. M. (1987). Direct measurement of suspended sediment transport, *Proceedings coastal sediments '87: ASCE*, pp. 723–737. New York
- Jaffe, B. E., Sternberg, R. W., & Sallenger, A. H. (1984). The role of suspended sediment in shore-normal beach profile change, *Proc. 19th Int. Coastal Eng. Conf.: ASCE* (pp. 1983–1996). New York. <https://doi.org/10.1061/9780872624382.134>
- Leatherman, S. P. (1976). Barrier island dynamics: Overwash processes and eolian transport. *Coastal Engineering Proceedings*, 1(15), 1958–1974. <https://doi.org/10.1061/9780872620834.114>
- Masselink, G., & van Heteren, S. (2014). Response of wave-dominated and mixed-energy barriers to storms. *Marine Geology*, 352, 321–347. <https://doi.org/10.1016/j.margeo.2013.11.004>
- Matias, A., Ferreira, A. S., Vila-Concejo, A., Morris, B., & Dias, J. A. (2009). Foreshore and hydrodynamic factors governing overwash. *Journal of Coastal Research*, 56, 636–640.
- Matias, A., Ferreira, Ó., Vila-Concejo, A., Morris, B., & Dias, J. A. (2010). Short-term morphodynamics of non-storm overwash. *Marine Geology*, 274(1), 69–84. <https://doi.org/10.1016/j.margeo.2010.03.006>
- Matias, A., Masselink, G., Kroon, A., Blenkinsopp, C. E., & Turner, I. L. (2013). Overwash experiment on a sandy barrier. *Journal of Coastal Research*, 1(65), 778. <https://doi.org/10.2112/si65-132.1>
- McCall, R. T., Plant, N., & Van Thiel de Vries, J. (2011). The effect of longshore topographic variation on overwash modelling. *Coastal Engineering Proceedings*, 1(32), 36. <https://doi.org/10.9753/icce.v32.sediment.36>
- McCall, R. T., Van Thiel De Vries, J. S. M., Plant, N. G., Van Dongeren, A. R., Roelvink, J. A., Thompson, D. M., & Reniers, A. J. H. M. (2010). Two-dimensional time dependent hurricane overwash and erosion modeling at Santa Rosa Island. *Coastal Engineering*, 57(7), 668–683. <https://doi.org/10.1016/j.coastaleng.2010.02.006>
- Mori, N., Suzuki, T., & Kakuno, S. (2007). Noise of acoustic Doppler velocimeter data in bubbly flows. *Journal of Engineering Mechanics*, 133(1), 122–125. [https://doi.org/10.1061/\(ASCE\)0733-9399\(2007\)133:1\(122\)](https://doi.org/10.1061/(ASCE)0733-9399(2007)133:1(122))
- Morton, R. A., & Sallenger, A. H. (2003). Morphological impacts of extreme storms on sandy beaches and barriers. *Journal of Coastal Research*, 19, 560–573. https://doi.org/10.1007/0-387-30843-1_51
- Nielsen, N., & Nielsen, J. (2006). Development of a washover fan on a transgressive barrier, Skallingen, Denmark. *Journal of Coastal Research*, 39, 107–111. https://doi.org/10.1007/springerreference_4799
- Oost, A. P., Hoekstra, P., Wiersma, A., Flemming, B., Lammerts, E. J., Pejrup, M., et al. (2012). Barrier island management: Lessons from the past and directions for the future. *Ocean & Coastal Management*, 68, 18–38. <https://doi.org/10.1016/j.ocecoaman.2012.07.010>
- Raubenheimer, B., Elgar, S., & Guza, R. T. (1998). Estimating wave heights from pressure measured in sand bed. *Journal of Waterway, Port, Coastal, and Ocean Engineering*, 124(3), 151–154. [https://doi.org/10.1061/\(ASCE\)0733-950X\(1998\)124:3\(151\)](https://doi.org/10.1061/(ASCE)0733-950X(1998)124:3(151))
- Ruessink, B. G. (2010). Observations of turbulence within a natural surf zone. *Journal of Physical Oceanography*, 40(12), 2696–2712. <https://doi.org/10.1175/2010JPO4466.1>
- Safak, I., Warner, J. C., & List, J. H. (2016). Barrier island breach evolution: Alongshore transport and bay-ocean pressure gradient interactions. *Journal of Geophysical Research: Oceans*, 121, 8720–8730. <https://doi.org/10.1002/2016JC012029>
- Sallenger Jr, A. H. (2000). Storm impact scale for barrier islands. *Journal of Coastal Research*, 16, 890–895. <https://doi.org/10.1306/44b4ba04-170a-11d7-8645000102c1865d>
- Sherwood, C. R., Long, J. W., Dickhudt, P. J., Dalyander, P. S., Thompson, D. M., & Plant, N. G. (2014). Inundation of a barrier island (Chandeleur Islands, Louisiana, USA) during a hurricane: Observed water-level gradients and modeled seaward sand transport. *Journal of Geophysical Research: Earth Surface*, 119, 1498–1515. <https://doi.org/10.1002/2013jf003069>
- Swart, D. (1974). A schematization of onshore-offshore transport. *Coastal Engineering Proceedings*, 1(14), 884–900. <https://doi.org/10.1061/9780872621138.054>
- Van Dongeren, A., & Van Ormondt, M. (2007). Hydrodynamic aspects of overwash. *Framework: H&I Zeereep (Report in Dutch)*, WL Delft Hydraulics, report Z, 4412, 33. https://doi.org/10.1142/9789814355537_0137
- Van Rijn, L. (1993). *Principles of sediment transport in rivers, estuaries and coastal seas*. Amsterdam, The Netherlands: Aqua Publications.
- Van der Vegt, M., & Hoekstra, P. (2012). Morphodynamics of a storm-dominated, shallow tidal inlet: The Slufter, the Netherlands. *Netherlands Journal of Geosciences*, 91(03), 325–339. <https://doi.org/10.1017/s0016774600000470>
- Wesselman, D., Winter, R., Engelstad, A., McCall, R., Dongeren, A., Hoekstra, P., et al. (2017). The effect of tides and storms on the sediment transport across a Dutch barrier island. *Earth Surface Processes and Landforms*, 43(3), 579–592. <https://doi.org/10.1002/esp.4235>